



Reduction of breathing artifacts in multifrequency magnetic resonance elastography of the abdomen

Mehrgan Shahryari¹  | Tom Meyer¹ | Carsten Warmuth¹ | Helge Herthum¹  | Gergely Bertalan¹ | Heiko Tzschätzsch¹ | Lisa Stencel¹ | Steffen Lukas¹ | Ledia Lilaj¹  | Jürgen Braun²  | Ingolf Sack¹ 

¹Department of Radiology, Charité–Universitätsmedizin Berlin, Berlin, Germany

²Institute of Medical Informatics, Charité–Universitätsmedizin Berlin, Berlin, Germany

Correspondence

Ingolf Sack, Department of Radiology, Charité–Universitätsmedizin Berlin, Charitéplatz 1, 10117 Berlin, Germany. Email: ingolf.sack@charite.de

Funding information The German Federal Ministry of Education and Research (LiSyM 031L0057) and the German Research Foundation (SFB1340 “Matrix in Vision” and GRK2260 BIOQIC)

Purpose: With abdominal magnetic resonance elastography (MRE) often suffering from breathing artifacts, it is recommended to perform MRE during breath-hold. However, breath-hold acquisition prohibits extended multifrequency MRE examinations and yields inconsistent results when patients cannot hold their breath. The purpose of this work was to analyze free-breathing strategies in multifrequency MRE of abdominal organs.

Methods: Abdominal MRE with 30, 40, 50, and 60 Hz vibration frequencies and single-shot, multislice, full wave-field acquisition was performed four times in 11 healthy volunteers: once with multiple breath-holds and three times during free breathing with ungated, gated, and navigated slice adjustment. Shear wave speed maps were generated by tomoelastography inversion. Image registration was applied for correction of intrascan misregistration of image slices. Sharpness of features was quantified by the variance of the Laplacian.

Results: Total scan times ranged from 120 seconds for ungated free-breathing MRE to 376 seconds for breath-hold examinations. As expected, free-breathing MRE resulted in larger organ displacements (liver, 4.7 ± 1.5 mm; kidneys, 2.4 ± 2.2 mm; spleen, 3.1 ± 2.4 mm; pancreas, 3.4 ± 1.4 mm) than breath-hold MRE (liver, 0.7 ± 0.2 mm; kidneys, 0.4 ± 0.2 mm; spleen, 0.5 ± 0.2 mm; pancreas, 0.7 ± 0.5 mm). Nonetheless, breathing-related displacement did not affect mean shear wave speed, which was consistent across all protocols (liver, 1.43 ± 0.07 m/s; kidneys, 2.35 ± 0.21 m/s; spleen, 2.02 ± 0.15 m/s; pancreas, 1.39 ± 0.15 m/s). Image registration before inversion improved the quality of free-breathing examinations, yielding no differences in image sharpness to uncorrected breath-hold MRE in most organs ($P > .05$).

Conclusion: Overall, multifrequency MRE is robust to breathing when considering whole-organ values. Respiration-related blurring can readily be corrected using image registration. Consequently, ungated free-breathing MRE combined with image registration is recommended for multifrequency MRE of abdominal organs.

This is an open access article under the terms of the Creative Commons Attribution License, which permits use, distribution and reproduction in any medium, provided the original work is properly cited.

© 2020 The Authors. *Magnetic Resonance in Medicine* published by Wiley Periodicals LLC on behalf of International Society for Magnetic Resonance in Medicine

KEYWORDS

abdomen, breathing artifacts, image registration, multifrequency MRE, navigator, stiffness

1 | INTRODUCTION

Abdominal magnetic resonance elastography (MRE) is gaining in importance for the clinical diagnosis of a large variety of diseases that alter the mechanical properties of tissues such as liver fibrosis,¹⁻⁵ portal hypertension,^{6,7} renal dysfunction,⁸⁻¹⁰ and tumors.¹¹⁻¹⁴ Since the introduction of MRE in 1995 by Muthupillai et al,¹⁵ various MRE methods tailored for clinical examinations of the abdomen have been proposed.¹⁶ A general challenge for abdominal MRE is to cope with respiratory motion during data acquisition, which potentially degrades the consistency of MRE-encoded vibration data.¹⁷ Therefore, the Quantitative Imaging Biomarkers Alliance of RSNA (Radiological Society of North America) recommends MRE of the liver to be performed during breath-holds after expiration.¹⁸ Standard MRE of the liver consists of acquisitions of four slices squeezed into multiple breath-holds of 12 to 20 seconds² or into a single breath-hold using rapid single-shot sequences or simultaneous multislice MRE.^{19,20} However, there are several reasons to avoid breath-holds in abdominal MRE. First, patients with chronic liver diseases often suffer from comorbidities that limit their ability to hold their breath after expiration during the acquisition of MRE data.¹⁷ Second, patients cannot always follow breathing commands, resulting in motion during scans or inconsistent organ positions.²¹ Furthermore, breath-holds might alter abdominal pressure and hepatic perfusion, which in turn affect liver stiffness.^{22,23} Finally, paused data acquisition to permit intermittent respiration prolongs total acquisition time beyond the clinically acceptable limit if rich data are acquired as in multifrequency, 3D MRE.

Published studies report multifrequency 3D MRE of abdominal organs with up to eight wave dynamics consecutively acquired at up to seven frequencies, resulting in total acquisition times exceeding 5 minutes, during which patients are allowed to breathe freely.^{8-10,24,25} The same protocol with breath-hold acquisition would exceed 20 minutes.²⁶ Nevertheless, there are good reasons for multifrequency MRE of abdominal organs, including measurement of viscoelastic dispersion or improved detail resolution.^{25,27,28} For example, tomoelastography, a multifrequency MRE technique for abdominal organs, was applied during free breathing for detecting small hepatic lesions¹⁴ or fine renal structures,²⁵ despite the risk of breathing artifacts. Although individual images from rapid single-shot MRE scans may have minimal motion artifacts in the organs of interest, intrascan misregistration may degrade the resulting elastograms. This study

addresses strategies to avoid and correct intrascan misregistration in single-shot MRE of abdominal organs. Our hypothesis is that detail resolution in multifrequency MRE can be further improved by suppression of motion artifacts either during image acquisition using respiratory navigators or with postprocessing using image registration before MRE wave inversion.

Experimental strategies include one-dimensional breathing navigators for either defining acquisition windows or for adapting slice positions following inspiration and expiration. Additionally, motion is corrected in raw MRI signals during postprocessing. These strategies will be compared with the current gold standard, which is breath-hold MRE. The overall aim of our study is to recommend strategies for efficiently suppressing breathing artifacts in abdominal multifrequency MRE toward time-efficient, highly resolved stiffness mapping of the liver, spleen, pancreas, and kidneys without the need for restricting breathing during the examination.

2 | METHODS

2.1 | Subjects and paradigms

Eleven healthy male participants (age, 28 ± 4 years; range, 23-38 years; body mass index, 23 ± 2 kg/m²) were included after approval by the institutional ethics review board of the Charité-Universitätsmedizin Berlin in accordance with the World Medical Association Declaration of Helsinki (Ethical Principles for Medical Research Involving Human Subjects). Written, informed consent was obtained. Volunteers reported no history of abdominal or respiratory diseases. Multifrequency MRE was conducted four times in each volunteer to investigate and compare the displacement of the liver, kidneys, spleen, and pancreas with use of different MRE protocols:

- (i) Block acquisitions during repeat breath-holds in expiration (BH-MRE);
- (ii) Continuous acquisitions during free breathing (FB-MRE);
- (iii) Continuous RF excitation (to maintain a steady state of magnetization) and gated block acquisition within an acquisition window (defined by the navigator signals through the diaphragm, G-MRE); and
- (iv) Continuous acquisitions during automated adjustments of image slice positions using a respiratory navigator within an acquisition window (gating and following, GF-MRE).

2.2 | Magnetic resonance imaging and MRE acquisition techniques

All MRI and MRE acquisitions were performed on a 1.5T clinical MRI scanner (Magnetom Sonata; Siemens, Erlangen, Germany) using a 12-channel phased-array surface coil and the spine-array coils integrated into the examination table. For anatomical orientation, localizer, T_1 -weighted and T_2 -weighted axial, as well as T_2 -weighted coronal MRI sequences were acquired before MRE. The MRE sequences and driver setups were similar to Shahryari et al.¹⁴ In brief, the driver setups consisted of four pressurized air drivers that were attached to the body surface with a Velcro belt at the position of the transpyloric plane. Two of the drivers were attached ventrally on the midclavicular line, while the remaining two were placed dorsally on the scapular line. Mechanical vibrations of 30, 40, 50, and 60 Hz frequency were induced in the abdomen with 0.4 bar air pressure for the ventral drivers and 0.6 bar air pressure for the dorsal drivers. Neither position nor air pressure of the actuators was individually adapted to the body shape of the volunteer. A single-shot spin-echo EPI sequence with flow-compensated motion-encoding gradients was used to acquire the 3D wave field.²⁹ Eight phase offsets over a full vibration period were recorded for all three Cartesian motion field directions. Nine contiguous slices of 5 mm thickness and placed in a coronal view through the liver, spleen, pancreas, and both kidneys were acquired, covering a FOV of $284 \times 350 \text{ mm}^2$. Further imaging parameters were as follows: matrix size = 104×128 , pixel resolution = $2.7 \times 2.7 \times 5 \text{ mm}^3$, TR = 1200 ms, TE = 55 ms, parallel imaging with GRAPPA factor 2, motion-encoding gradient frequency = 43.48 Hz for 30, 40, and 50 Hz vibration frequencies and 44.88 Hz for 60 Hz vibration frequency, and motion-encoding gradient amplitude = 30 mT/m.

For BH-MRE (i), single-component, single-frequency MRE data of each of the three Cartesian wave field components and four drive frequencies were acquired block-wise. Therefore, separate scans were performed during 12 single breath-holds in expiration of approximately 10 seconds duration. Data were merged afterward to full six-dimensional data arrays of sizes $104 \times 128 \times 9 \times 8 \times 3 \times 4$, depicting 3D spatial-resolved displacement data ($104 \times 128 \times 9$) at multiple time steps (8), components (3), and frequencies (4) resulting in $N = 96$ consecutively acquired slice blocks. The magnitude images of the 96 acquired slice blocks were averaged to a mean magnitude image (M). For FB-MRE (ii), all data were continuously acquired without account of respiratory motion.

For G-MRE (iii) and GF-MRE (iv), we integrated a navigator echo into the EPI-MRE sequence before slice block acquisition, to monitor the respiratory position based on the method described in Henningsson and Botnar.³⁰ In brief, a pencil beam RF pulse with 30° flip angle and 20 mm diameter was positioned craniocaudally through the right

diaphragm with the readout axis parallel to the long axis of the beam. The acquired navigator data were then Fourier-transformed in real time, generating a one-dimensional line image illustrating respiratory motion. An acceptance window of 5 mm has been defined for G-MRE to interrupt the acquisition of data outside this window. In GF-MRE, the acceptance window was 20 mm, within which the position of the full image slice block was continuously moved along the head-to-foot axis, to follow the position of the right diaphragm depicted by the navigator signal. As in G-MRE, data acquisition was interrupted if a very deep breathing motion exceeded the 20 mm window detected by the navigator. Of note, image slices were continuously excited in G-MRE and GF-MRE, similar to FB-MRE but with paused data acquisition whenever the navigator signal was outside the acceptance window. Because TR in all protocols was identical (1.2 seconds), a similar steady state of magnetization was established during FB-MRE, G-MRE, and GF-MRE. Only in BH-MRE did the steady-state magnetization have to be re-established for each single breath-hold, potentially inducing MRI intensity fluctuations. However, as analyzed later, these fluctuations did not affect the sharpness of averaged magnitude images M. All protocols are illustrated in Figure 1.

2.3 | Magnetic resonance elastography data processing

Organ displacement and motion artifacts were quantified by 2D rigid-body image registration using the open-source *Elastix* toolbox.³¹ Therefore, a presegmentation region of interest (ROI) was manually delineated for each organ, covering the full organ with a tolerance margin of approximately 5 pixels that covers organ displacements caused by motion. Presegmentation ROIs for image registration are demarcated in Supporting Information Figure S1. The mean MRE magnitude images (M) displaying a mixed T_2 and T_2^* contrast were registered to the first of $8 \times 3 \times 4 = 96$ slice blocks acquired during a multifrequency MRE scan using (1) advanced Mattes mutual information with 32 histogram bins as a similarity metric³² and (2) stochastic gradient descent as an optimizer implemented in *Elastix*. The registration was performed with a pyramid resampling scheme at three different resolutions. The optimizer was set to a maximum of 100 iterations, and at each iteration, 2000 random coordinates were sampled for the computation of the similarity metric. As a result, $N = 95$ in-plane relative displacements x (horizontally) and y (vertically) were generated for each organ. Mean displacement U was then calculated by taking the mean of the magnitude displacements $u_n = \sqrt{(\bar{x} - x_n)^2 + (\bar{y} - y_n)^2}$, with the bar denoting time-averaged displacements x and y . For motion correction, third-order B-spline interpolation was

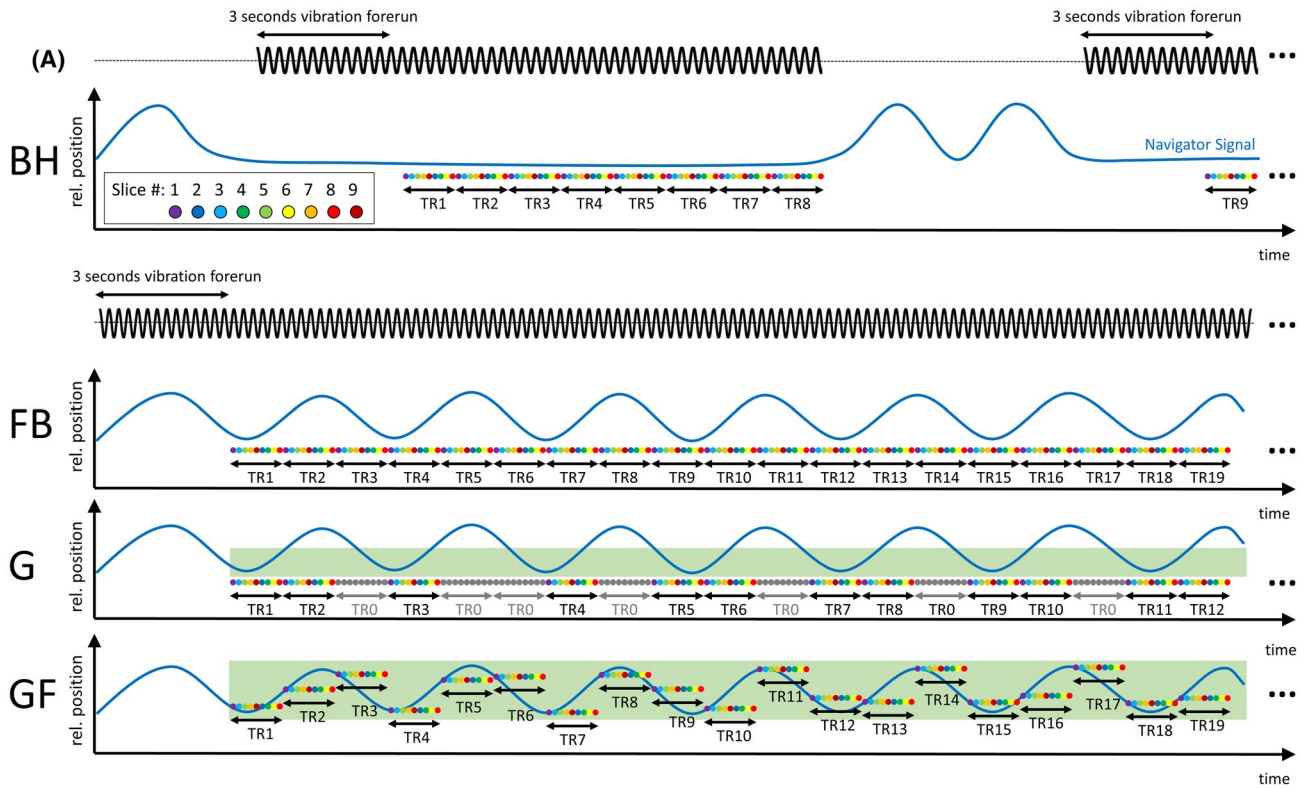


FIGURE 1 Schematic timing of magnetic resonance elastography (MRE) protocols tested in this study. A, Breath-hold MRE (BH) with acquisition of slice blocks during repeat breath-holds in expiration. B, Continuous free-breathing MRE: ungated (FB), gated by respiratory navigator signals (G), and with automated adjustment of image slice positions according to the navigator signal (GF). Shown is the relative timing of vibration along with the relative position (rel. position) of navigator signals along the craniocaudal axis through the diaphragm. The timing of slice acquisition and slice positions (on rel. position axis) are indicated by colored circles. Vibrations were induced 3 seconds before data acquisition, to establish a steady-state flux of shear waves throughout the abdomen. Note that slices are acquired in an interleaved manner in the following order: 1, 3, 5, 7, 9, 2, 4, 6, 8. TR1, TR2, and so on, denote the TRs of each block of nine image slices. The gray circles during TR0 indicate that the data acquisition was interrupted (due to the respiration detected by the navigator), whereas the RF stimulation was performed continuously. After measuring TR1-TR8 with the first motion-encoding gradient (MEG) component, the following 16 TRs are measured with the second and third MEG, respectively

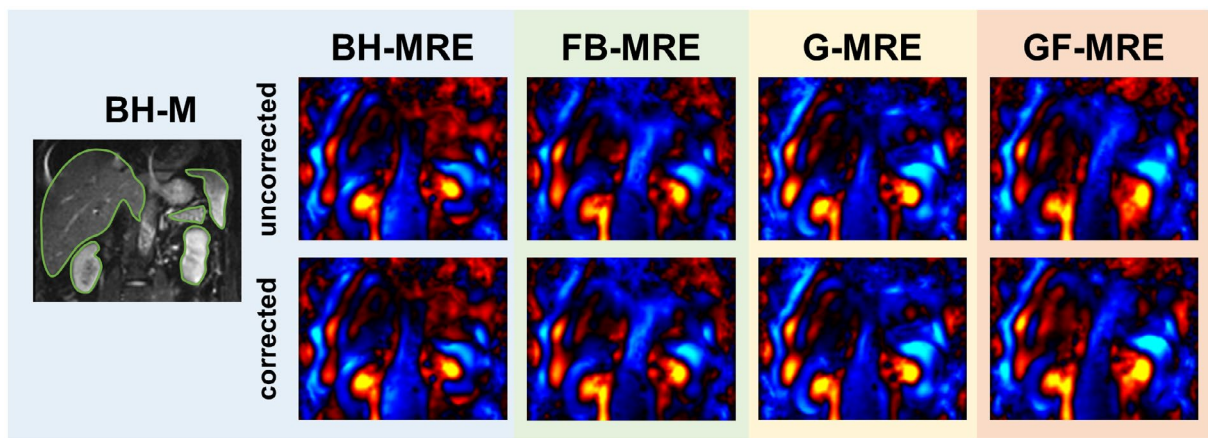


FIGURE 2 Wave images acquired in a volunteer in a coronal view through the liver, pancreas, spleen, and kidneys with 40 Hz excitation frequency (left–right deflection component) after unwrapping and temporal Fourier transformation, uncorrected and corrected for motion using image registration. Blue to yellow colors scale the deflections from left to right with amplitudes of 20 μm . A magnitude image (gray scale) from breath-hold MRE (BH-MRE) is shown for anatomical orientation and display of organ-specific regions of interest (green lines). Abbreviations: FB-MRE, ungated free-breathing MRE; G-MRE, gated free-breathing MRE; GF-MRE, gated, slice-following, free-breathing MRE

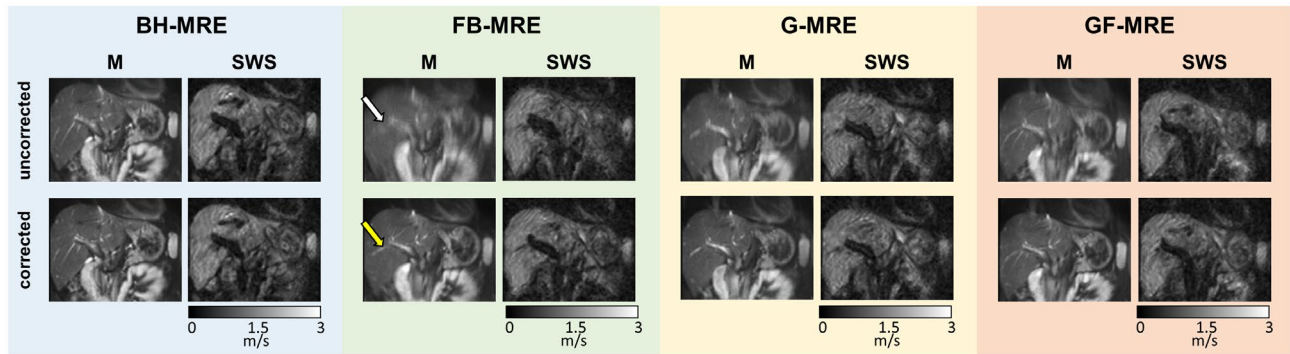


FIGURE 3 Representative magnitude MRE images (magnitude [M], T_2 , and T_2^* weighted) and stiffness maps (shear wave speed [SWS]) of the liver of a healthy subject obtained with different MRE protocols. Shown are averaged images with and without correction for breathing artifact by 2D in-plane rigid registration. Open arrow indicates blurred features, and yellow arrow indicates improved anatomical representations

used to apply the transformations to the real and imaginary parts of the complex MRI data, the phases of which were further processed for MRE parameter recovery. Although no explicit smoothing step was implemented in the registration process, a slight smoothing may have occurred due to the B-spline interpolation.

Figure 2 shows representative 40 Hz waves (left-to-right component) in a slice covering the liver, kidneys, spleen, and pancreas acquired with all MRE protocols, uncorrected and corrected. More material on animated waves is presented in Supporting Information Video S1. All MRE wave data were processed using wave number-based multifrequency dual elasto-visco inversion (k-MDEV), which provides maps of the shear wave speed (SWS) in meters per second.³³ Because SWS is derived from the real part of wave numbers, it is virtually not influenced by viscosity and can be considered a surrogate of stiffness. The inversion pipeline is publicly available at <https://bioqic-apps.charite.de>.³⁴ For parameter quantification, organ-specific ROIs were manually drawn based on time-averaged magnitude MRE (M) images and accounting for whole-organ boundaries, as illustrated in Figure 2. Furthermore, these ROIs were refined by empirical thresholds of 1 m/s for softer organs (liver and pancreas) and 1.5 m/s for stiffer organs (spleen and kidneys), to remove blood vessels that appear enlarged in SWS maps.^{24,35} Without motion, both M (MRE magnitude averaged over 96 consecutively acquired image slice blocks) and SWS maps are expected to display sharp edges at tissue interfaces, which is reflected in the Laplacian Δ of the images. Therefore, image sharpness was quantified by computing the variance (σ) of the Laplacian Δ of MRE images as described in Pech-Pacheco et al.³⁶ A Laplacian derivative kernel of size 3×3 was applied to both the mean magnitude M (averaged over 96 image slice blocks) and SWS maps. The value of σ was then derived by computing the variance of ΔM and ΔSWS within presegmented ROIs of each organ and protocol.

2.4 | Statistical analysis

The mean U, SWS, and sharpness (σ) were calculated for all four breathing paradigms and organs. All values are tabulated as mean \pm SD, unless otherwise stated. Statistical significance of differences in displacement and stiffness across all abdominal organs and motion-reduction strategies (protocols) were analyzed using linear mixed-effect models. Linear mixed-effect models accounted for U and SWS as dependent variables, whereas organs and protocols, as well as their interactions, were taken as independent variables. Statistical differences of the dependent variables were tested by Tukey's post hoc test with Bonferroni correction for multiple comparisons. A paired Student t-test was used to test for differences between uncorrected and motion-corrected MRE data based on SWS values. A Wilcoxon signed-rank test was used to test for differences between uncorrected and motion-corrected σ in all organs and protocols. Furthermore, the same test was applied to test for differences between uncorrected BH-MRE and motion-corrected FB-MRE, as well as motion-corrected BH-MRE and motion-corrected FB-MRE in all organs.

The significance level was set to 5%. Statistical analysis was performed in R (version 3.6.2; R-Foundation, Vienne, Austria) using "lme4," "lsmeans," and "ggplot2" packages.

3 | RESULTS

Figures 3-6 illustrate the effects of breathing motion and artifact-reduction strategies in different organs of 1 representative volunteer. Participant characteristics and group mean values of U, SWS, and σ of ΔM and SWS of all abdominal organs and protocols are summarized in Table 1. Scan times were 376 ± 68 seconds for BH-MRE, 120 seconds for FB-MRE, 166 ± 117 seconds for G-MRE, and 128 ± 17 seconds for GF-MRE. In addition to total acquisition time, it took 168 seconds on average (range, 18-413 seconds) to set up the respiratory navigators for G-MRE and GF-MRE.

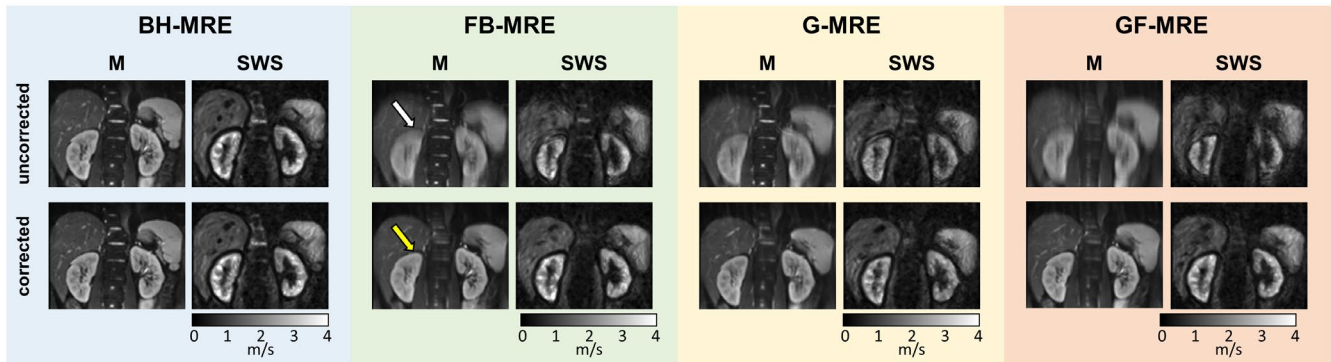


FIGURE 4 Representative magnitude MRE images (M, T_2 , and T_2^* weighted) and stiffness maps (SWS) of the kidneys of a healthy subject obtained with different MRE protocols. Shown are averaged images with and without correction for breathing artifact by 2D in-plane rigid registration. Open arrow indicates blurred features, and yellow arrow indicates improved anatomical representations

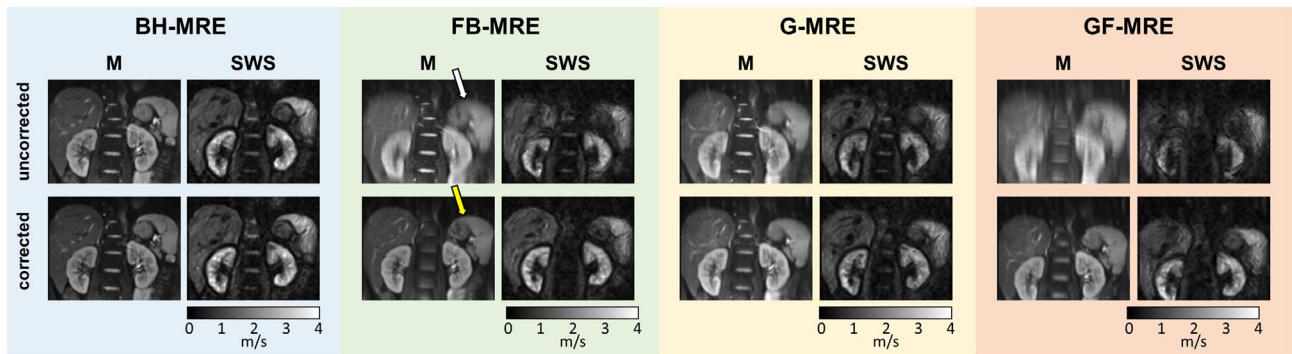


FIGURE 5 Representative magnitude MRE images (M, T_2 , and T_2^* weighted) and stiffness maps (SWS) of the spleen of a healthy subject obtained with different MRE protocols. Shown are averaged images with and without correction for breathing artifact by 2D in-plane rigid registration. Open arrow indicates blurred features, and yellow arrow indicates improved anatomical representations

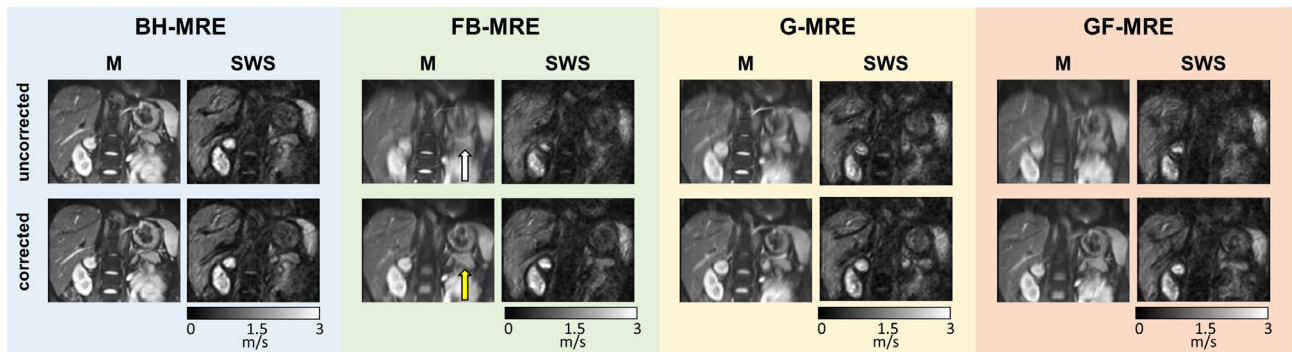


FIGURE 6 Representative magnitude MRE images (M, T_2 , and T_2^* weighted) and stiffness maps (SWS) of the pancreas of a healthy subject obtained with different MRE protocols. Shown are averaged images with and without correction for breathing artifact by 2D in-plane rigid registration. Open arrow indicates blurred features, and yellow arrow indicates improved anatomical representations

3.1 | Displacement

The BH-MRE protocol was used as reference standard for the four abdominal organs investigated by multifrequency MRE. There were only minor displacements of these organs (liver, 0.7 ± 0.2 mm; kidneys, 0.4 ± 0.2 mm; spleen,

0.5 ± 0.2 mm; pancreas, 0.7 ± 0.5 mm) without significant differences among them (all $P > .05$). In FB-MRE, the liver was most severely affected by displacement (liver, 4.7 ± 1.5 mm; kidneys, 2.4 ± 2.2 mm; spleen, 3.1 ± 2.4 mm; pancreas, 3.4 ± 1.4 mm) with significantly larger displacement amplitudes than the kidneys ($P < .01$). Navigated GF-MRE

TABLE 1 Group mean values of organ displacement, sharpness, and stiffness obtained with different multifrequency MRE protocols (mean value ± SD)

Organ	Protocol	U (mm)	σ of ΔM		SWS (m/s)		σ · 10 ⁻² of ΔSWS				
			Uncorrected	Corrected	P-Values	Uncorrected	Corrected	P-Values	Uncorrected	Corrected	P-Values
Liver	BH-MRE	0.7 ± 0.2	45.9 ± 30.7	51.5 ± 26.0	ns	1.49 ± 0.11	1.49 ± 0.12	ns	1.05 ± 0.16	1.06 ± 0.16	ns
	FB-MRE	4.7 ± 1.5	24.3 ± 14.1	37.8 ± 23.7	< .001	1.44 ± 0.07	1.43 ± 0.07	ns	0.99 ± 0.13	0.97 ± 0.09	ns
	G-MRE	3.5 ± 1.4	29.4 ± 17.6	45.7 ± 27.6	.003	1.46 ± 0.09	1.46 ± 0.09	ns	0.99 ± 0.13	1.03 ± 0.18	ns
	GF-MRE	2.6 ± 1.4	40.2 ± 29.8	42.3 ± 30.4	ns	1.45 ± 0.07	1.45 ± 0.07	ns	0.98 ± 0.15	0.99 ± 0.15	ns
Kidneys	BH-MRE	0.4 ± 0.2	372.1 ± 149.2	430.7 ± 149.8	< .001	2.46 ± 0.25	2.46 ± 0.24	ns	4.04 ± 1.11	4.19 ± 1.23	.042
	FB-MRE	2.4 ± 2.2	174.7 ± 62.2	231.8 ± 96.9	.014	2.33 ± 0.22	2.35 ± 0.21	ns	3.26 ± 0.79	3.42 ± 0.76	ns
	G-MRE	2.0 ± 1.7	213.4 ± 125.9	262.6 ± 145.7	.002	2.34 ± 0.20	2.35 ± 0.20	ns	3.27 ± 0.87	3.37 ± 0.90	ns
	GF-MRE	5.6 ± 2.6	136.1 ± 98.9	255.6 ± 138.6	.002	2.34 ± 0.18	2.36 ± 0.17	ns	3.06 ± 0.53	3.34 ± 0.55	.003
Spleen	BH-MRE	0.5 ± 0.2	465.0 ± 350.6	539.5 ± 400.1	ns	2.02 ± 0.18	2.03 ± 0.18	ns	7.12 ± 3.98	7.49 ± 3.92	ns
	FB-MRE	3.1 ± 2.4	314.9 ± 354.1	438.1 ± 459.4	.005	2.01 ± 0.17	2.02 ± 0.15	ns	5.99 ± 3.17	6.56 ± 4.03	ns
	G-MRE	3.0 ± 1.8	417.0 ± 474.0	530.0 ± 573.6	< .001	2.02 ± 0.17	2.00 ± 0.17	ns	6.84 ± 3.98	7.22 ± 4.44	.042
	GF-MRE	5.9 ± 3.8	349.8 ± 380.6	509.5 ± 509.9	.003	2.01 ± 0.20	2.02 ± 0.20	ns	6.51 ± 3.76	6.85 ± 4.19	ns
Pancreas	BH-MRE	0.7 ± 0.5	642.4 ± 265.2	839.8 ± 518.3	.042	1.38 ± 0.15	1.41 ± 0.16	ns	6.97 ± 3.01	6.94 ± 2.95	ns
	FB-MRE	3.4 ± 1.4	310.1 ± 224.2	548.6 ± 390.2	< .001	1.36 ± 0.14	1.39 ± 0.15	ns	5.33 ± 2.24	5.81 ± 2.41	.007
	G-MRE	3.0 ± 1.3	338.4 ± 251.3	491.3 ± 326.5	.019	1.38 ± 0.14	1.37 ± 0.12	ns	5.31 ± 1.81	5.74 ± 2.29	ns
	GF-MRE	5.0 ± 2.6	280.6 ± 280.4	519.0 ± 507.3	.014	1.37 ± 0.12	1.39 ± 0.13	ns	6.09 ± 2.34	5.95 ± 1.61	ns

Note: P-values refer to tests uncorrected versus corrected. Abbreviation: ns, not significant.

reduced liver displacement relative to FB-MRE to 2.6 ± 1.4 mm ($P = .011$), while displacement of the other organs remained unchanged or even increased (kidneys, 5.6 ± 2.6 mm, $P < .001$; spleen, 5.9 ± 3.8 mm, $P < .001$; pancreas, 5.0 ± 2.6 mm, $P = .063$; P -values relative to FB-MRE). Larger displacement amplitudes in these organs compared with the liver were consistent with an increased latency between navigator scans and more posterior slices (eg, slice 7, 400 ms; slice 9, 533 ms; slice 6, 933 ms; and slice 8, 1067 ms, in the interleaved multislice acquisition scheme illustrated in Figure 1). Displacement was slightly better for G-MRE, which acquired data during relatively quiet phases of breathing only. Here, displacement improved relative to GF-MRE for three organs (kidneys, 2.0 ± 1.7 mm, $P < .001$; spleen, 3.0 mm \pm 1.8, $P < .001$; pancreas, 3.0 ± 1.3 mm, $P = .013$), whereas liver displacement did not significantly change (3.5 ± 1.4 mm, $P = .538$) despite significantly longer acquisition. The results are summarized in Table 1. Statistical plots of U for all organs and protocols are shown in Figure 7.

3.2 | Stiffness

Figure 8 presents organ-specific differences in SWS with mean values of 1.43 ± 0.07 m/s (liver), 2.35 ± 0.21 m/s (kidneys), 2.02 ± 0.15 m/s (spleen), and 1.39 ± 0.15 m/s

(pancreas) obtained during free breathing (all $P < .001$, except for liver vs. pancreas: $P > .05$). Interestingly, SWS did not differ across protocols despite the aforementioned differences in U (all $P > .05$).

3.3 | Sharpness

Sharpness was improved by image registration as revealed to the naked eye when looking at both MRE magnitude images (M) and SWS maps (Figure 3-6). Accordingly, σ of ΔM showed a significant reduction of blurring after registration in all organs investigated for FB-MRE and G-MRE (all $P < .05$). Registration improved the GF-MRE data obtained in the kidneys, spleen, and pancreas (all $P < .05$), whereas the liver, analyzed based on the first slice, had lower displacement amplitudes in GF-MRE and did not benefit from registration. Interestingly, sharpness even improved in BH-MRE examinations for the kidneys and pancreas, indicating the susceptibility of these organs to unconscious motion during breath-holds (Figure 9). After motion correction of FB-MRE, σ was indistinguishable from uncorrected BH-MRE in the liver, spleen, and pancreas (all $P > .05$), while corrected FB-MRE in the kidneys had still lower σ -values than uncorrected BH-MRE ($P < .01$) despite visual improvements. Motion-corrected BH-MRE shows significantly higher

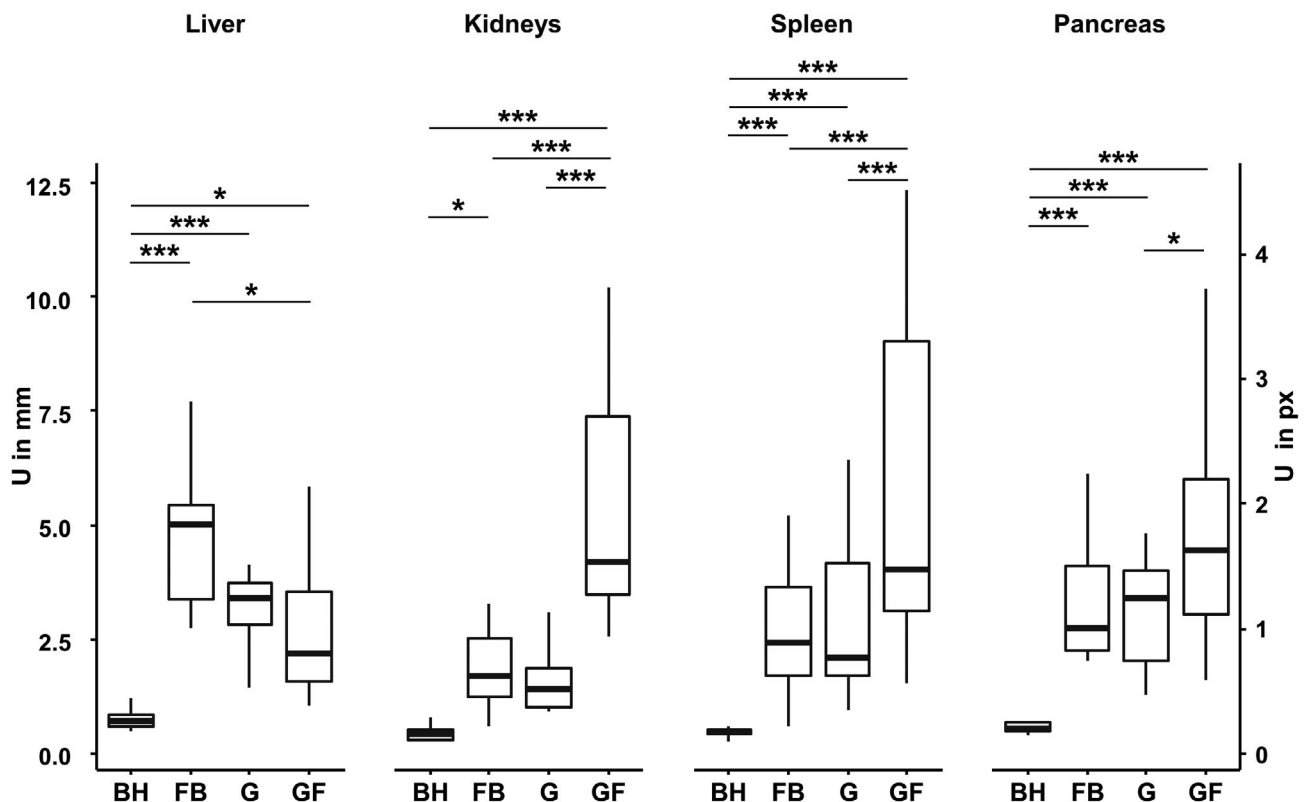


FIGURE 7 Group statistical plots of displacement amplitudes U (in millimeters and in pixels) of the liver, kidneys, spleen, and pancreas for different MRE protocols (* $P < .05$, ** $P < .01$, *** $P < .001$)

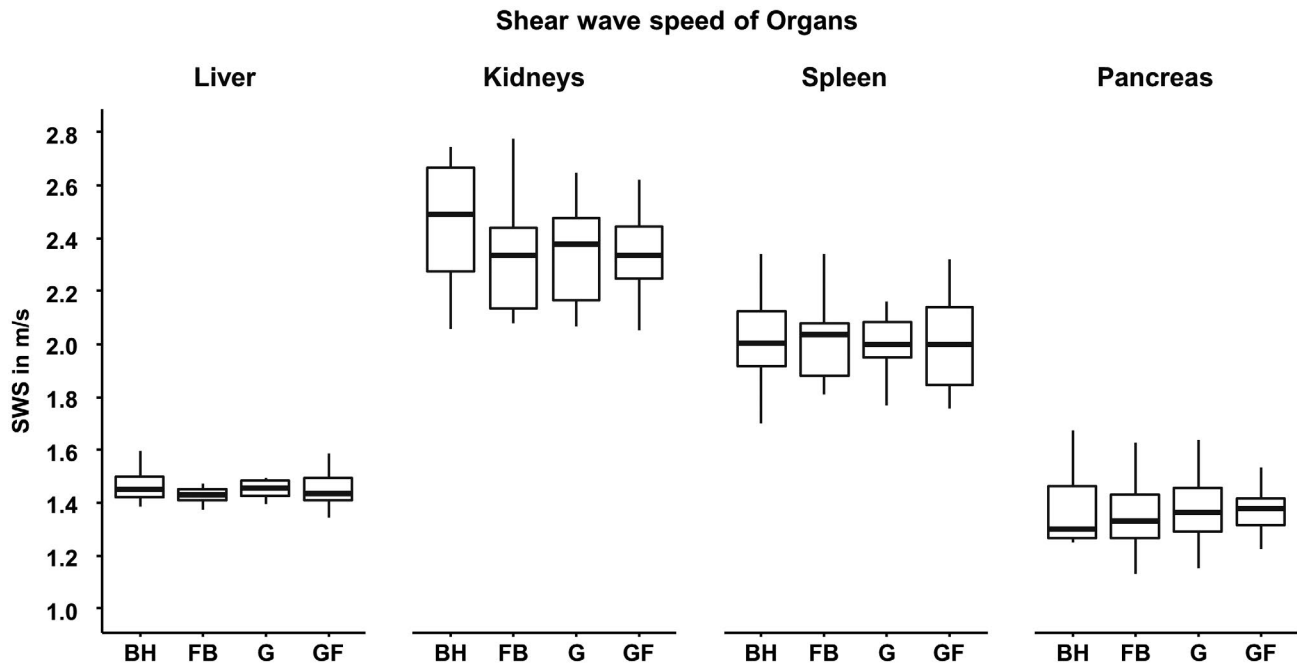


FIGURE 8 Group statistical plots of stiffness SWS (in meters per second) of the liver, kidneys, spleen, and pancreas for different MRE protocols

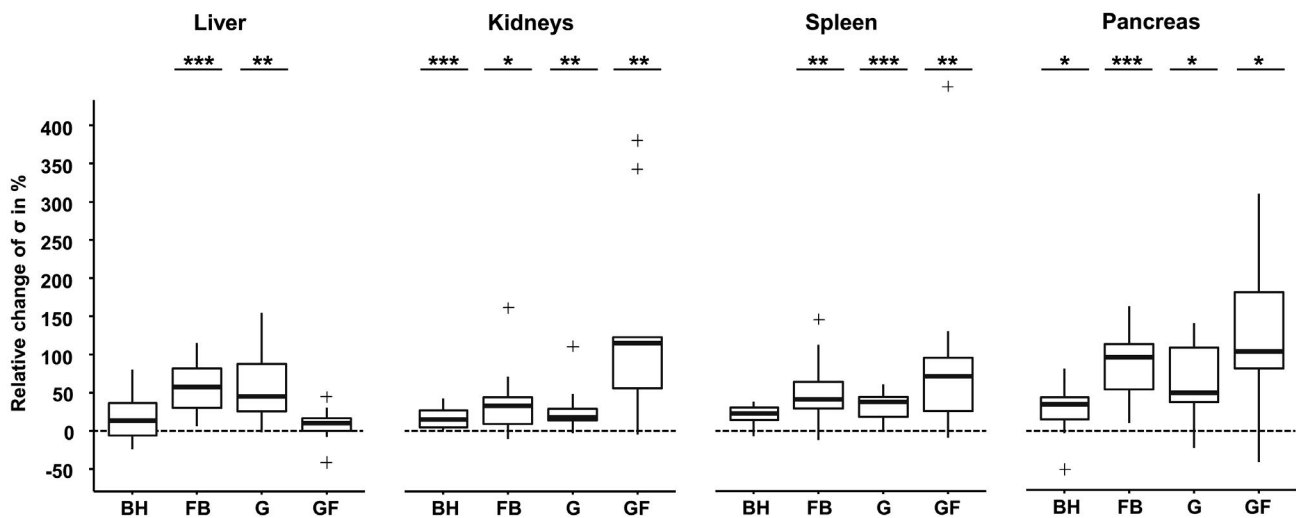


FIGURE 9 Box plot of relative changes of image sharpness (in percentages) indicated by the sharpness variance σ ($[\sigma(\text{corrected}) - \sigma(\text{uncorrected})] / \sigma(\text{uncorrected}) \cdot 100$) of the Laplacian Δ of MRE magnitude ($*P < .05$, $**P < .01$, $***P < .001$)

σ values compared with motion-corrected FB-MRE in the liver, kidneys, and pancreas (all $P < .05$), whereas no such difference to the spleen was observed. Representative ΔM and ΔSWS images are shown in Supporting Information Figure S1. It is apparent from the examples shown that ΔSWS improved primarily at organ boundaries, indicating sharper edges while within organs, and higher-frequency ΔSWS patterns are seemingly unaffected by the image registration.

All relevant parameters are summarized in Table 1.

4 | DISCUSSION AND CONCLUSIONS

This study of breathing-induced artifacts in multifrequency MRE presents three key findings. First, this is the first study providing systematic quantitative motion data for different abdominal organs when asymptomatic subjects freely breathe during MRE data acquisition with different protocols. Second, our results demonstrate that averaged MRE values are surprisingly stable, regardless of whether

MRE is performed during free breathing or breath-holds. Finally, we show that un navigated free-breathing MRE combined with motion correction by image registration represents the optimal trade-off in terms of scan time and detail resolution. In the following, we will briefly discuss each of these three points.

- (i) Breath-hold MRE results in the smallest displacement amplitudes of abdominal organs compared with free-breathing MRE and navigator-triggered gating MRE techniques. The liver and pancreas are the abdominal organs most severely affected by breathing, whereas the kidneys show the smallest displacement amplitudes. An earlier study of our group shows that multifrequency MRE of the kidneys is improved when omitting any breathing command compared with breath-hold MRE.²⁵ However, this case-specific finding from a single subject was never reproduced or compared with other abdominal organs, as done in the present study.
- (ii) All protocols provided values in the range of published values of abdominal MRE (converting SWS to shear modulus by $\mu = \text{SWS}^2 \cdot 1000 \text{ kg/m}^3$)³⁷⁻³⁹ or directly agreed with reported SWS values in that region.^{25,40} The visible blurring of the magnitude images in free-breathing MRE (see Figures 3-6) suggests that stiffness values are strongly affected by breathing motion, which, however, is not the case. This observation is remarkable because it indicates the intrinsic stability of MRE to respiration.^{41,42} We attribute this stability to two main effects. First, MRE analyzes parameters that refer to local wavelengths, which in turn are unaffected by boundary conditions to a certain extent. Although actuator position, wave amplitudes, and wave patterns can change with breathing, the resulting parameter maps do not necessarily reflect these changes. Second, local wavelengths are calculated from time-harmonic tissue displacements selected from the fundamental frequency in the Fourier spectrum.¹⁶ This is temporal filtering, which efficiently suppresses breathing-related signals as long as they do not overlap with the timing of the fundamental oscillation. For these reasons, MRE might be more robust to breathing-induced artifact than other MRI techniques. Because the MRE magnitude signals presented in Figures 3-6 are time-averaged across 96 consecutive acquisitions, similar blurring would occur in any MRI data acquired over the same time during free breathing.
- (iii) Nonetheless, blurring can sufficiently be corrected by image registration. The resulting improvement in sharpness σ was seen primarily in magnitude images, and to a lesser extent in stiffness maps. The SWS maps predominantly suffered from distorted boundaries,

which became sharper after correction, although without significant changes in σ . Therefore, we may conclude that σ of SWS maps tends to exaggerate degradation of images by possible artifacts. For example, breathing-related organ displacement causes high-frequency SWS changes, which are spuriously interpreted by σ as sharpness. Despite the inappropriateness of σ to reflect improvements in stiffness maps, the facts that MRE magnitude images are significantly improved (as correctly quantified by σ) and that anatomical organ boundaries are more conspicuous in SWS maps after image registration (as revealed to the eye when looking at the SWS maps in Figures 3-6) suggest image registration to be a feasible way of reducing motion artifacts in multifrequency MRE.

In essence, we recommend free-breathing multifrequency MRE in conjunction with retrospective rigid-body image registration for abdominal tomoelastography, as it combines the shortest acquisition times with preserved sharpness of organ boundaries and tissue interfaces.

Our study has limitations. First, our displacement analysis was essentially 2D. Given that major breathing motion occurred along the craniocaudal axis,⁴³ which is covered by coronal view, our 2D in-plane motion correction was effective. However, through-plane motion occurring in transverse orientation needs to be addressed by rigid 3D image registration. Second, our navigator-based motion-correction technique uses single navigators in conjunction with subsequent full-slice block acquisition. For that reason, early slices acquired immediately after the navigators are more reliable than late slices due to the latency between navigator signal and slice acquisition. In our setup, liver motion was evaluated in the first slice, which was well addressed by GF-MRE. However, GF-MRE was less efficient in organs other than the liver, which were covered by images slices acquired at later time points. Although adaptation of slice positions is possible to focus on other organs, we do not recommend GF-MRE but rather FB-MRE combined with image registration. Third, as mentioned previously, Laplacian Δ and variance σ are limited in assessing sharpness of stiffness (SWS) maps. A suitable parameter for the future assessment of detail resolution in MRE should quantify the sharpness of tissue boundaries rather than higher frequency features in SWS maps. Future research in MRE is warranted to identify such a measure of sharpness of elastograms. Ideally, such a measure should afford quantitative assessment of image quality in MRE and ultimately allow automated detection of reliable maps⁴⁴ and reduction of technical failures.⁴⁵ Finally, we focused here on SWS as a surrogate of stiffness but did not analyze viscosity-related parameters such as wave penetration,³³ damping ratio,⁴⁶ loss modulus,¹¹ and loss angle or fluidity.¹⁴ However, we assume that our analysis of breathing

artifacts can also be applied to other mechanical parameters attainable by MRE.


In summary, we have introduced and compared different motion-artifact reduction strategies in multifrequency MRE with the aims of testing the susceptibility of MRE to breathing motion and proposing a time-efficient multifrequency MRE protocol that generates reliable stiffness maps. Our findings indicate that larger displacement amplitudes due to respiratory motion do not significantly affect averaged MRE values and that breathing motion can readily be corrected by image registration, which improves both the sharpness and detail resolution of MRE magnitude images and parameter maps. Consequently, the shortest free-breathing protocol is recommended for 3D multifrequency MRE of the abdomen and allows stiffness mapping without breathing commands in approximately 2 minutes.

ACKNOWLEDGMENTS

We gratefully acknowledge the support of the German Federal Ministry of Education and Research (LiSyM 031L0057) and the German Research Foundation (SFB1340 “Matrix in Vision” and GRK2260 BIOQIC). Open access funding enabled and organized by Projekt DEAL.

ORCID

Mehrgan Shahryari  <https://orcid.org/0000-0002-3981-1711>

Helge Herthum  <https://orcid.org/0000-0001-6494-0833>

Ledia Lilaj  <https://orcid.org/0000-0001-8222-0397>

Jürgen Braun  <https://orcid.org/0000-0001-5183-7546>

Ingolf Sack  <https://orcid.org/0000-0003-2460-1444>

REFERENCES

- Venkatesh SK, Yin M, Ehman RL. Magnetic resonance elastography of liver: Technique, analysis, and clinical applications. *J Magn Reson Imaging*. 2013;37:544-555.
- Venkatesh SK, Ehman RL. Magnetic resonance elastography of abdomen. *Abdom Imaging*. 2015;40:745-759.
- Garteiser P, Doblbas S, Van Beers BE. Magnetic resonance elastography of liver and spleen: Methods and applications. *NMR Biomed*. 2018;31:e3891.
- Huwart L, Sempoux C, Salameh N, et al. Liver fibrosis: Noninvasive assessment with MR elastography versus aspartate aminotransferase-to-platelet ratio index. *Radiology*. 2007;245:458-466.
- Yin M, Talwalkar JA, Glaser KJ, et al. Assessment of hepatic fibrosis with magnetic resonance elastography. *Clin Gastroenterol Hepatol*. 2007;5:1207-1213.e1202.
- Guo J, Buening C, Schott E, et al. In vivo abdominal MR elastography for the assessment of portal hypertension before and after transjugular intrahepatic portosystemic shunt (TIPS) implantation. *Investigative Radiology*. 2015;50:347-351.
- Navin PJ, Gidener T, Allen AM, et al. The role of magnetic resonance elastography in the diagnosis of noncirrhotic portal hypertension. *Clin Gastroenterol Hepatol*. 2019;s1542-3565(19)31162-0.
- Marticorena Garcia SR, Fischer T, Durr M, et al. Multifrequency magnetic resonance elastography for the assessment of renal allograft function. *Invest Radiol*. 2016;51:591-595.
- Lang ST, Guo J, Bruns A, et al. Multiparametric quantitative MRI for the detection of IgA nephropathy using tomoelastography, DWI, and BOLD imaging. *Invest Radiol*. 2019;54:669-674.
- Marticorena Garcia SR, Grossmann M, Bruns A, et al. Tomoelastography paired with T2* magnetic resonance imaging detects lupus nephritis with normal renal function. *Invest Radiol*. 2019;54:89-97.
- Garteiser P, Doblbas S, Daire JL, et al. MR elastography of liver tumours: Value of viscoelastic properties for tumour characterisation. *Eur Radiol*. 2012;22:2169-2177.
- Shi Y, Gao F, Li Y, et al. Differentiation of benign and malignant solid pancreatic masses using magnetic resonance elastography with spin-echo echo planar imaging and three-dimensional inversion reconstruction: A prospective study. *Eur Radiol*. 2018;28:936-945.
- Gordic S, Ayache JB, Kennedy P, et al. Value of tumor stiffness measured with MR elastography for assessment of response of hepatocellular carcinoma to locoregional therapy. *Abdom Radiol (NY)*. 2017;42:1685-1694.
- Shahryari M, Tzschatzsch H, Guo J, et al. Tomoelastography distinguishes noninvasively between benign and malignant liver lesions. *Cancer Res*. 2019;79:5704-5710.
- Muthupillai R, Lomas DJ, Rossman PJ, Greenleaf JF, Manduca A, Ehman RL. Magnetic resonance elastography by direct visualization of propagating acoustic strain waves. *Science*. 1995;269:1854-1857.
- Hirsch S, Braun J, Sack I. *Magnetic Resonance Elastography: Physical Background and Medical Applications*. Weinheim, Germany: Wiley-VCH; 2017:456.
- Murphy IG, Graves MJ, Reid S, et al. Comparison of breath-hold, respiratory navigated and free-breathing MR elastography of the liver. *Magn Reson Imaging*. 2017;37:46-50.
- QIBA MR Elastography Biomarker Committee. Magnetic Resonance Elastography of the Liver, Quantitative Imaging Biomarkers Alliance. 2. Profile Stage: Consensus. QIBA, June 6, 2019. <http://qibawiki.rsna.org/index.php/Profiles>. Accessed January 4, 2020.
- Majeed W, Kalra P, Kolipaka A. Simultaneous multislice rapid magnetic resonance elastography of the liver. *NMR Biomed*. 2020;33:e4252.
- Ebersole C, Ahmad R, Rich AV, Potter LC, Dong H, Kolipaka A. A Bayesian method for accelerated magnetic resonance elastography of the liver. *Magn Reson Med*. 2018;80:1178-1188.
- Kennedy P, Wagner M, Castera L, et al. Quantitative elastography methods in liver disease: Current evidence and future directions. *Radiology*. 2018;286:738-763.
- Ipek-Ugay S, Tzschatzsch H, Braun J, Fischer T, Sack I. Physiologic reduction of hepatic venous blood flow by the Valsalva Maneuver decreases liver stiffness. *J Ultrasound Med*. 2017;36:1305-1311.
- Millonig G, Friedrich S, Adolf S, et al. Liver stiffness is directly influenced by central venous pressure. *J Hepatol*. 2010;52:206-210.
- Hudert CA, Tzschatzsch H, Rudolph B, et al. Tomoelastography for the evaluation of pediatric nonalcoholic fatty liver disease. *Invest Radiol*. 2019;54:198-203.
- Marticorena Garcia SR, Grossmann M, Lang ST, et al. Tomoelastography of the native kidney: Regional variation and physiological effects on in vivo renal stiffness. *Magn Reson Med*. 2018;79:2126-2134.
- Hirsch S, Guo J, Reiter R, et al. MR elastography of the liver and the spleen using a piezoelectric driver, single-shot wave-field

- acquisition, and multifrequency dual parameter reconstruction. *Magn Reson Med.* 2014;71:267-277.
27. Asbach P, Klatt D, Schlosser B, et al. Viscoelasticity-based staging of hepatic fibrosis with multifrequency MR elastography. *Radiology.* 2010;257:80-86.
 28. Etehall E, Juge L, Hatt A, Sinkus R, Bilston LE. Liver stiffness values are lower in pediatric subjects than in adults and increase with age: A multifrequency MR elastography study. *Radiology.* 2017;283:222-230.
 29. Dittmann F, Reiter R, Guo J, et al. Tomoelastography of the prostate using multifrequency MR elastography and externally placed pressurized-air drivers. *Magn Reson Med.* 2018;79:1325-1333.
 30. Henningsson M, Botnar RM. Advanced respiratory motion compensation for coronary MR angiography. *Sensors (Basel).* 2013;13:6882-6899.
 31. Klein S, Staring M, Murphy K, Viergever MA, Pluim JP. elastix: A toolbox for intensity-based medical image registration. *IEEE Trans Med Imaging.* 2010;29:196-205.
 32. Mattes D, Haynor DR, Vesselle H, Lewellen TK, Eubank W. PET-CT image registration in the chest using free-form deformations. *IEEE Trans Med Imaging.* 2003;22:120-128.
 33. Tzschatzsch H, Guo J, Dittmann F, et al. Tomoelastography by multifrequency wave number recovery from time-harmonic propagating shear waves. *Med Image Anal.* 2016;30:1-10.
 34. Meyer T, Tzschätzsch H, Braun J, Kalra P, Kolipaka A, Sack I. Online platform for extendable server-based processing of magnetic resonance elastography data. In: Proceedings of the 27th Annual Meeting of ISMRM, Montreal, Canada, 2019. Abstract. 3966.
 35. Reiter R, Tzschatzsch H, Schwahofer F, et al. Diagnostic performance of tomoelastography of the liver and spleen for staging hepatic fibrosis. *Eur Radiol.* 2020;30:1719-1729.
 36. Pech-Pacheco JL, Cristobal G, Chamorro-Martinez J, Fernandez-Valdivia J. Diatom autofocusing in brightfield microscopy: a comparative study. In: Proceedings of the 15th International Conference on Pattern Recognition, Barcelona, Spain, 2000. pp 314-317.
 37. Gandhi D, Kalra P, Raterman B, Mo X, Dong H, Kolipaka A. Magnetic resonance elastography of kidneys: SE-EPI MRE reproducibility and its comparison to GRE MRE. *NMR Biomed.* 2019;32:e4141.
 38. Gandhi D, Kalra P, Raterman B, Mo X, Dong H, Kolipaka A. Magnetic resonance elastography-derived stiffness of the kidneys and its correlation with water perfusion. *NMR Biomed.* 2020;33:e4237.
 39. Kolipaka A, Schroeder S, Mo X, Shah Z, Hart PA, Conwell DL. Magnetic resonance elastography of the pancreas: Measurement reproducibility and relationship with age. *Magn Reson Imaging.* 2017;42:1-7.
 40. Dittmann F, Tzschatzsch H, Hirsch S, et al. Tomoelastography of the abdomen: Tissue mechanical properties of the liver, spleen, kidney, and pancreas from single MR elastography scans at different hydration states. *Magn Reson Med.* 2017;78:976-983.
 41. Glaser KJ, Chen J, Ehman RL. Fast 2D hepatic MR elastography for free-breathing and short breath hold applications. In: Proceedings of the 24th Annual Meeting of ISMRM, Singapore, 2015. Abstract 2522.
 42. Li J, Dzyubak B, Glaser KJ, et al. Repeatability and clinical performance of non-gated, free-breathing, MR elastography (MRE) of the liver. In: Proceedings of the 27th Annual Meeting of ISMRM, Montreal, Canada, 2019. Abstract 3972.
 43. Brandner ED, Wu A, Chen H, et al. Abdominal organ motion measured using 4D CT. *Int J Radiat Oncol Biol Phys.* 2006;65:554-560.
 44. Dzyubak B, Venkatesh SK, Manduca A, Glaser KJ, Ehman RL. Automated liver elasticity calculation for MR elastography. *J Magn Reson Imaging.* 2016;43:1055-1063.
 45. Kim DW, Kim SY, Yoon HM, Kim KW, Byun JH. Comparison of technical failure of MR elastography for measuring liver stiffness between gradient-recalled echo and spin-echo echo-planar imaging: A systematic review and meta-analysis. *J Magn Reson Imaging.* 2020;51:1086-1102.
 46. Yin M, Glaser KJ, Manduca A, et al. Distinguishing between hepatic inflammation and fibrosis with MR elastography. *Radiology.* 2017;284:694-705.

SUPPORTING INFORMATION

Additional supporting information may be found online in the Supporting Information section.

FIGURE S1 Representative Laplacian images of magnetic resonance elastography (MRE) magnitude (ΔM) and shear wave speed (ΔSWS) of the liver, kidneys, spleen, and pancreas of a healthy subject obtained with different MRE protocols. Shown are images with and without correction for breathing artifacts by 2D in-plane rigid registration. Green contours show the presegmented region of interest used for image registration. Arrows indicate blurred features (open arrows) and improved anatomical representations (yellow arrows) in each organ. Note that improved feature sharpness is better seen in ΔM than in ΔSWS . The ΔSWS maps reveal high-frequency patterns (eg, red arrows) that do not change with correction and therefore hinder quantification of sharpness by σ . Abbreviations: BH-MRE, breath-hold MRE; FB-MRE, ungated free-breathing MRE; G-MRE, gated free-breathing MRE; GF-MRE, gated, slice-following, free-breathing MRE

VIDEO S1 Animated wave images acquired in a volunteer in a coronal view through the liver, pancreas, spleen, and kidneys for all excitation frequencies (30–60 Hz) and deflection components (left–right, head–feet, through-plane) after unwrapping and temporal Fourier transformation, uncorrected and corrected for motion using image registration. Blue to yellow colors scale deflections with amplitudes of 30 and 20 μm for 30 and 40 Hz, respectively, and 15 μm for 50 and 60 Hz. Mean magnitude images (M) in gray scale of the respective mechanical frequency are shown for anatomical orientation and display of organ-specific regions of interest (green lines). In the shown cases, image registration for motion correction was applied to the spleen

How to cite this article: Shahryari M, Meyer T, Warmuth C, et al. Reduction of breathing artifacts in multifrequency magnetic resonance elastography of the abdomen. *Magn Reson Med.* 2021;85:1962–1973. <https://doi.org/10.1002/mrm.28558>